

Using the Long Wavelength Array to Search for Cosmic Dawn

CHRISTOPHER DiLULLO ¹, GREGORY B. TAYLOR ¹, AND JAYCE DOWELL ¹

¹*University of New Mexico
210 Yale Blvd. NE
Albuquerque, NM 87131*

ABSTRACT

The search for the spectral signature of hydrogen from the formation of the first stars, known as Cosmic Dawn or First Light, is an ongoing effort around the world. The signature should present itself as a decrease in the temperature of the 21-cm transition relative to that of the Cosmic Microwave Background and is believed to reside somewhere below 100 MHz. A potential detection was published by the Experiment to Detect the Global EoR Signal (EDGES) collaboration with a profile centered around 78 MHz of both unexpected depth and width (Bowman et al. 2018). If validated, this detection will have profound impacts on the current paradigm of structure formation within Λ CDM cosmology. We present an attempt to detect the spectral signature reported by the EDGES collaboration with the Long Wavelength Array station located on the Sevilleta National Wildlife Refuge in New Mexico, USA (LWA-SV). LWA-SV differs from other instruments in that it is a 256 element antenna array and offers beamforming capabilities that should help with calibration and detection. We report first limits from LWA-SV and look toward future plans to improve these limits.

1. INTRODUCTION

The spin-flip transition in neutral hydrogen provides the opportunity to study the ionization history of the Universe via its corresponding 21-cm emission. This transition occurs when an electron in the 1S ground state changes from having its spin parallel to that of the proton to antiparallel. The small energy difference between these configurations corresponds to a photon with a wavelength of 21.1 cm, or a frequency of 1420 MHz. This provides a useful probe for observing the early Universe where neutral hydrogen is abundant. See Furlanetto et al. (2006); Morales & Wyithe (2010); Pritchard & Loeb (2012) for an in-depth review of cosmology using the 21-cm line.

The formation of the first stars, known as Cosmic Dawn, marks the beginning of a phase transition for the Universe where it changes from being predominately neutral beforehand to predominately ionized after the Epoch of Reionization (EoR). Tracing the relative brightness of the 21-cm emission, with respect to the Cosmic Microwave Background (CMB) as a function of redshift, gives insight into which processes dominate the excitation state of the hydrogen during times when the first structures are forming in the Universe. The differential brightness temperature of the 21-cm signal relative to the CMB, δT_B , can be shown to follow:

$$\delta T_B \approx 27 \cdot x_{HI} \sqrt{\frac{1+z}{10}} \left(\frac{T_S - T_{CMB}}{T_S} \right) \text{mK}, \quad (1)$$

where T_S is the spin temperature of the hydrogen, T_{CMB} is the temperature of the CMB, and x_{HI} is the fraction of neutral hydrogen (Pritchard & Loeb 2012). These quantities are all highly dependent on redshift, z . We have ignored terms dealing with spatial density fluctuations.

The driving factor that determines the detectability of the 21-cm transition, either as absorption or emission relative to the CMB, at a given redshift is the spin temperature of the hydrogen, which describes the relative population difference between the parallel and antiparallel spin states. The spin temperature is affected by three main processes: absorption and emission of 21-cm photons, collisions with other hydrogen atoms and with free electrons, and resonant

scattering of Ly α photons that can induce a spin-flip, known as the Wouthuysen-Field effect (Wouthuysen 1952; Field 1958).

It is expected that the ultraviolet radiation from the first stars couples to the surrounding neutral hydrogen via the Wouthuysen-Field effect. This decouples the HI spin temperature from the temperature of the CMB and instead couples it to the colder kinetic temperature of the gas. The kinetic temperature of the gas, T_K , is colder than that of the CMB, T_γ , since $T_K = T_0(1+z)$ for a non-relativistic gas, but $T_\gamma = T_0(1+z)^2$ for photons, where T_0 is the respective temperature of each measured in the current epoch. This would drive the spin temperature to be less than T_{CMB} and so, from Equation 1, the 21-cm signal is expected to show in absorption against the CMB for these redshifts. Astrophysical properties of the early Universe correlated with the features of the 21-cm signal suggest that the absorption feature should be present at frequencies less than 100 MHz (Cohen et al. 2017). While most experiments have historically focused on detecting the later EoR emission signal, experiments around the world are beginning to look for this absorption feature as well (e.g. Sokolowski et al. 2015; Singh et al. 2018; Price et al. 2018). These experiments rely on using a small number of elements to observe the entire sky and return the sky-averaged spectrum.

After the first galaxies begin to form, their UV flux ionizes regions of the surrounding medium. This heating drives the 21-cm signal into emission and the signal becomes dominated by the filling fraction of HII regions (Furlanetto et al. 2004). Experiments attempting to measure the three-dimensional k-space power spectrum of the 21-cm line at these redshifts are searching for this emission signal (e.g. Parsons et al. 2010; Harker et al. 2010; DeBoer et al. 2017).

The Experiment to Detect the Global EoR Signal (EDGES) collaboration has published a potential detection of the absorption signal from Cosmic Dawn (Bowman et al. 2018). They have reported a flattened Gaussian profile centered at 78.1 MHz with a width of 18.7 MHz and an amplitude of 0.53 K. Both the shape and amplitude of this profile is unexpected from conventional models (Furlanetto 2006) and, if validated, could imply interactions between baryons and dark matter (Barkana 2018; Muñoz & Loeb 2018; Berlin et al. 2018) or the presence of an unaccounted component in the radio background at these redshifts (Feng & Holder 2018; Mirocha & Furlanetto 2018; Dowell & Taylor 2018). There has also been much debate in the validity of this profile (Hills et al. 2018; Bradley et al. 2019; Singh & Subrahmanyan 2019; Sims & Pober 2019). This debate, coupled with the wide ranging implications of this potential detection, warrants a follow up with a different instrument in order to validate the reported profile parameters. The Long Wavelength Array (LWA) offers an opportunity for follow up as the profile center of 78.1 MHz falls within its observable band of 10-88 MHz. The full LWA currently consists of 3 stations: LWA1, which is colocated with the Karl J. Jansky Very Large Array in New Mexico, USA; LWA-SV, which is located on the Sevilleta National Wildlife Refuge in New Mexico, USA; and LWA-OVRO, which is located at the Owens Valley Radio Observatory in the Owens Valley, California, USA. The constituent stations can operate independently and offer a beamforming mode which is described in this paper.

The work detailed in this paper uses LWA-SV, which is the second station of the larger Long Wavelength Array. The beamforming mode of LWA-SV offers a new method for detecting the potential Cosmic Dawn signal. As mentioned above, other experiments that are searching for this signal observe the entire sky and generate sky-averaged spectra. This can create challenges as sources of contamination, namely extragalactic point sources and galactic synchrotron and free-free emission, can obscure the signal. The beamforming capability of LWA-SV allows for spatial selection on the sky in order to avoid sources of contamination, such as bright sources and the Galactic plane. This will not fully remove contamination, since the beam side lobes will pick up some unwanted signal, but it should improve overall performance. Beamforming also allows us to try a different method for calibrating the array, namely simultaneously observing a bright calibrator source with a second beam. This allows for *in situ* astronomical calibration of the entire system instead of relying on laboratory measurements like other experiments.

2. THE LONG WAVELENGTH ARRAY

LWA-SV (Taylor et al. 2012; Cranmer et al. 2017) is an antenna array consisting of 256 dual-polarization antennas which are arranged in a pseudo-random layout and observe within the frequency range 3-88 MHz. It can support two simultaneous beam pointings with each beam containing two tunings with 9.8 MHz of bandwidth¹. The array is roughly 110 m \times 100 m in the N/S and E/W directions, respectively.

¹ LWA-SV has been upgraded since this work was completed. It now supports three simultaneous beams with each beam containing two tunings with 19.6 MHz of bandwidth.

Table 1. Radiometer Equation Assumptions and Results for $T_{rms} = 50$ mK.

ν	$\Delta\nu$	A_e	T_{sys}	Δt
55 MHz	9.57 kHz	1900 m ²	3840 K	73.4 s
65 MHz	9.57 kHz	1360 m ²	2500 K	32.0 s
75 MHz	9.57 kHz	1020 m ²	1740 K	15.5 s

The system must be stable in time in order to integrate the data long enough to achieve significant signal to noise. If the system is not stable, fluctuations in the data can obscure the signal as the data is averaged over times longer than the fluctuation timescale. Single element experiments suffer from the need for integration times on the order of hours. However, LWA-SV benefits from its large effective area and should be able to reach a residual r.m.s of 50 mK, one tenth of the signal amplitude reported by the EDGES collaboration, within an integration time of 10's of seconds and so the electronics are not required to be stable over large fractions of a day or over multiple days. We estimate this using the radiometer equation within the Rayleigh-Jeans limit to relate integration time to an observed brightness temperature via:

$$\Delta t = \frac{1}{2\Delta\nu} \left[\frac{c^2 T_{sys}}{\nu^2 T_{rms} A_e} \right]^2, \quad (2)$$

where $\Delta\nu$ is the channel bandwidth, ν is the tuning frequency, A_e is the effective area of the array, and T_{sys} and T_{rms} are the system and r.m.s. brightness temperatures, respectively. Assumed values² for a few frequencies and results for the integration time are summarized in Table 1.

The signal chain of LWA-SV is straight forward, but there are many places that can introduce instabilities. The entire chain can be broken into the front end electronics (FEEs) and the back end electronics. The FEEs are dual polarization receiver boards located on each of the dipoles. They provide initial amplification and low-pass filtering of the signal before it is passed to the back end electronics. The back end of LWA-SV consists of two components, the analogue signal processor (ASP) and the advanced digital processor (ADP). The ASP electronics apply a second gain stage to the dual polarization analogue signal from each dipole and apply a bandpass to the signal. These signals are then passed along to ROACH-2 boards within ADP which digitize them and compute the Fast Fourier Transform (FFT) in order to output a complex spectrum. These data are then passed into the beamformer, after which the full beamformed data is recorded onto disk.

To ensure that the data remains unobscured by any fluctuations in the electronics chain of LWA-SV, we verified that an unstructured noise signal injected into the back end electronics integrated as expected. A Noisecom, Inc. model 3201K³ noise source was connected to one input of ASP and all other inputs were zero weighted. The choice of which ASP input channel the noise source is injected into should not affect the results. The ASP electronics are designed to have channel independent outputs and this has been verified through lab measurements⁴. If the station is generally stable over a given length of time, the data output by the system for a noise-like input should integrate with an r.m.s. which goes like:

$$\sigma \propto t^{-1/2}, \quad (3)$$

since this is true for Gaussian data. It is important to note that this only tests the stability of the back end electronics and does not account for potential instabilities in the FEE.

Temperature variations in the electronics shelter, due to the air conditioning cycle, cause the amplifier responses in the electronics to vary creating power variations in the data. We correct for these variations by fitting a linear relation between the observed median drift and the median temperature of the ASP electronics which is used to detrend the observed drift. The detrended drifts are then multiplied by the mean power of the original drift. The linear fit and drifts, before and after correction, are shown in Figures 1 and 2, respectively.

² <http://lwa.phys.unm.edu/obsstatus/obsstatus006.html#toc14>

³ <https://www.noisecom.com/products/calibrated-sources/nc3200-coaxial-noise-sources>

⁴ See LWA Memo #201

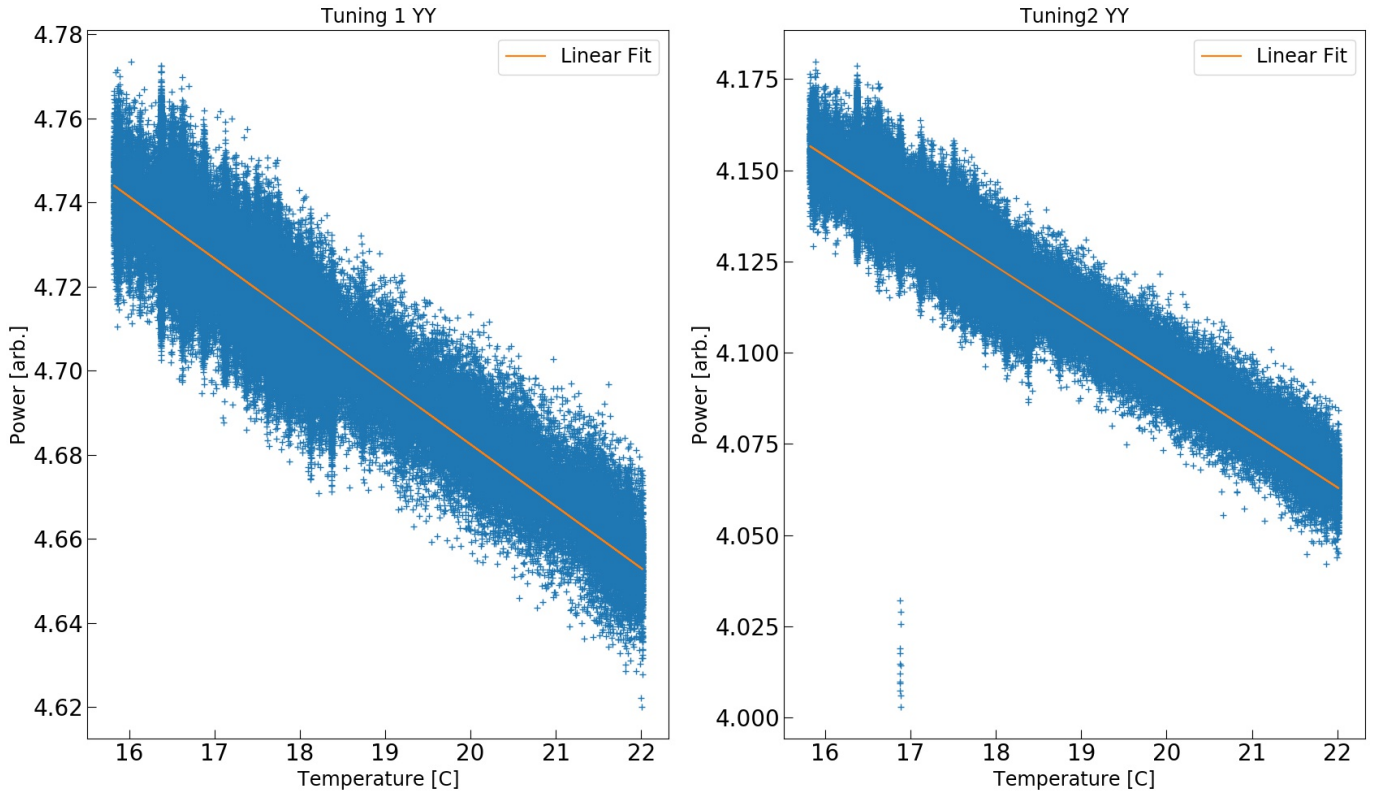


Figure 1. Median power across frequency vs ASP electronics temperature. The linear fit is used to detrend air conditioning cycle effects.

After correcting for power variations induced by the air conditioning cycle, we iteratively compute the r.m.s. noise of the data at different integration times to test overall system performance. In order to test how the data as a whole integrates, we use a bootstrapping method to randomly select 75% of frequency channels at each iteration. We then compute the r.m.s. in each of these channels and report the mean r.m.s. noise for that integration time. The results are shown in Figure 3 for integration times up to 24 minutes. We fit a line using the data for integration times of $t \leq 120$ s and report the best fit slopes. It is apparent that while we do not integrate down with the ideal slope of -0.5 (see Equation 3), we have good performance with slopes that are ~ 0.05 away from ideal. It is unclear why we begin to plateau after integration times larger than a few minutes. The larger variations in the curves at the largest integration times are likely statistical in origin. The uncertainty in the r.m.s. at these integrations is dominated by statistical uncertainty arising from small sampling size. A 4 hour observation will only have 10 data points with which to compute the r.m.s. for an integration time of 24 minutes. We conclude that the system is stable at least on the order of a few minutes. This should be enough to detect the Cosmic Dawn signal (see Table 1).

3. OBSERVATIONS

The LWA1 Low Frequency Sky Survey (LFSS; Dowell et al. 2017) covered the entire sky visible to the LWA and was used to identify the coldest region on the sky. The reasoning for this was to minimize foreground contamination. The coldest region on the sky should offer the best chance to disentangle the Cosmic Dawn signal from galactic foregrounds. The cold region that was identified and observed has J2000 coordinates of a RA of $9^{\text{h}} 38^{\text{m}} 40.56^{\text{s}}$ and a DEC of $+30^{\circ} 49' 1.4''$, hereafter referred to as the “Science Field”. In order to calibrate the observations, we simultaneously point a second beam at Virgo A, located at J2000 coordinates of a RA of $12^{\text{h}} 30^{\text{m}} 49.42^{\text{s}}$ and a DEC of $+12^{\circ} 23' 28''$. This allows for simultaneous *in situ* calibration using a source which $\sim 43.7^{\circ}$ away on the sky. This helps calibrate out time dependent systematics. The angular separation between Virgo A and the Science Field is large which means that this calibration will not accurately account for ionospheric effects since the two beams will each suffer unique perturbations as the signal paths through the ionosphere are different. This can be addressed with

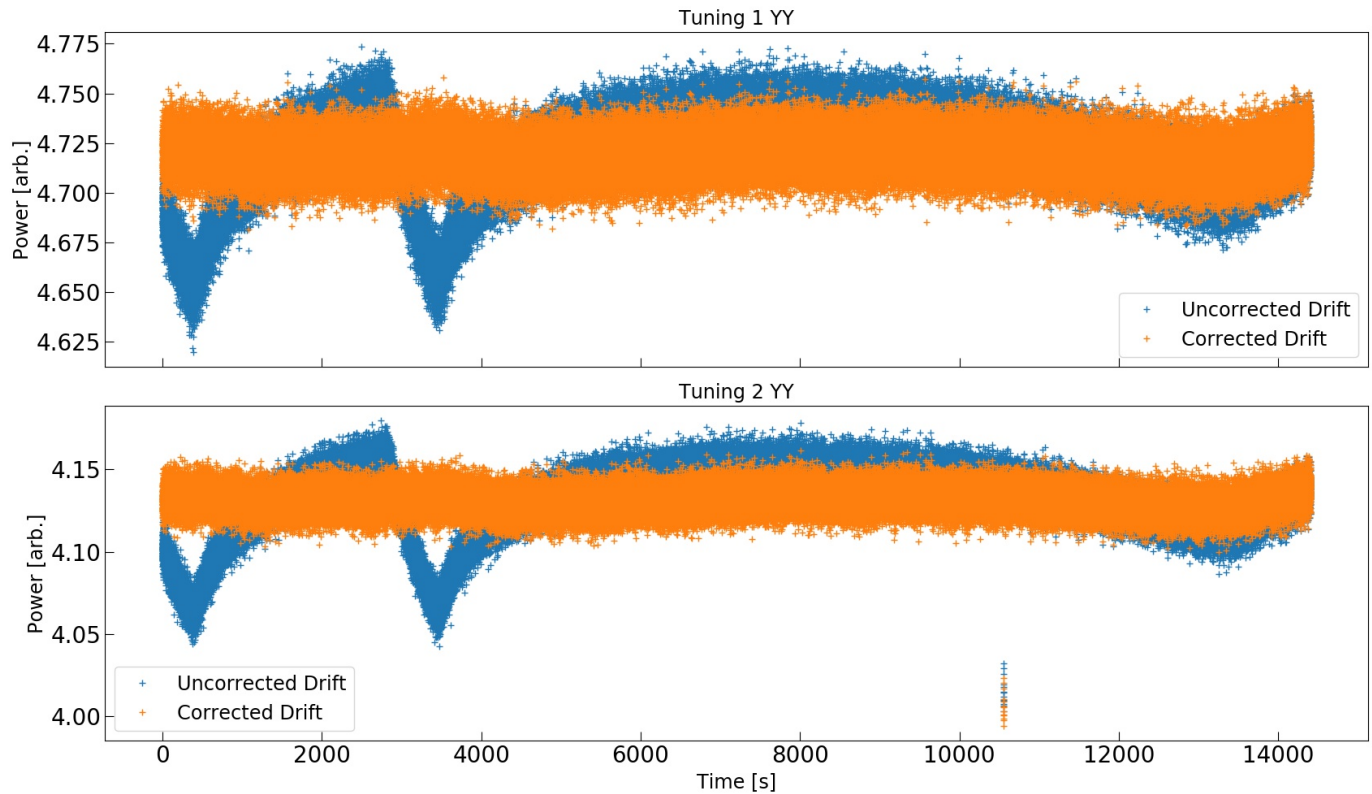


Figure 2. Uncorrected and corrected median drifts. The uncorrected drifts have large temporal structure in them as a result of the air conditioning cycle within the electronics shelter of LWA-SV. This causes variations in the response of the ASP electronics which induce power variations. The corrected drifts have been detrended and are centered about the mean of the uncorrected drifts.

an ionospheric model, but that will be considered in the future. However, Virgo A is the closest object which is also significantly bright enough to use for calibration.

Observations were taken on 2019, October 11th for 3 hours beginning at 15:58:00 UTC. This time range captures both Virgo A and the Science Field at high elevation, with their elevations being similar during the midpoint of the observation. This minimizes any elevation dependent effects during the middle of the observation. Both beams contain two tunings centered at 67 and 75 MHz, each with a bandwidth of 9.8 MHz. Accounting for rolloff at the edges of the band, which limits us to the inner 80%, this yields almost continuous coverage between 63 and 79 MHz. There is a small gap in coverage with a width of about 0.5 MHz around 71 MHz.

We chose LWA-SV’s spectrometer mode⁵, which channelizes the data and averages individual integrations to output time averaged spectra, for data acquisition. Setting the number of frequency channels to 1024 and the number of integrations per spectrum to 768 provided us with spectra with 9.56 kHz frequency resolution and 80 ms time resolution. We obtained spectra for the two linear polarizations XX and YY, which are elongated in the E/W and N/S directions, respectively. All data reduction was done using modules in the LWA Software Library⁶(LSL; Dowell et al. 2012).

We flag RFI using a pseudo-spectral kurtosis flagging criterion (Nita & Gary 2010a,b) that flags data with a spectral kurtosis outside of $3\text{-}\sigma$ from the mean. The spectral kurtosis is “pseudo” because the spectra that is output by the spectrometer mode is an average over our chosen number of 768 integrations per spectrum. We also use a smooth-bandpass model, created by smoothing the data along the frequency axis, to flag any frequency channels with an average power greater than $15\text{-}\sigma$ from the mean. This helps flag narrow-band RFI arising from digital television pilot tones that fall within the observed band that are not captured by the pseudo-spectral kurtosis criterion. One RFI

⁵ See LWA Memo #177.

⁶ <http://fornax.phys.unm.edu/lwa/trac/wiki>

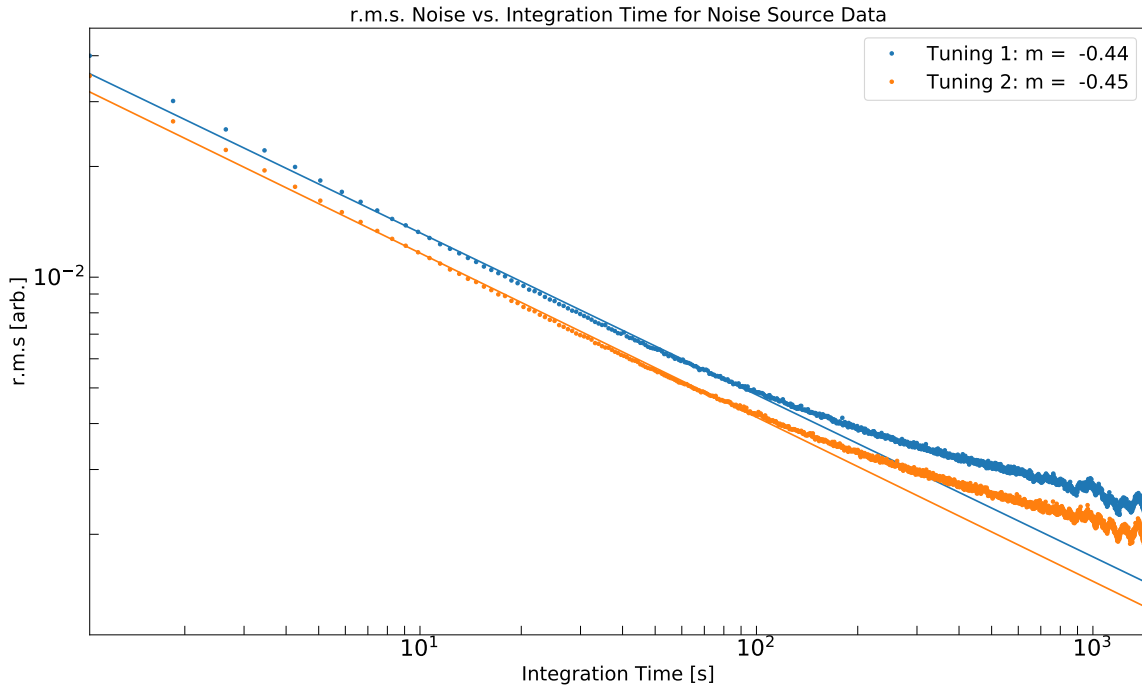


Figure 3. Log-log plot of r.m.s. noise vs integration time for a Gaussian noise source. Unstructured Gaussian data should integrate down with a slope of -0.5 . The linear fits are computed over times $t \leq 120$ s.

source was identified as originating from a noisy electrical pole located roughly a mile from the station, but it is unclear what effect this has on the overall quality of the data.

The spectra output by LWA-SV are initially in units of power on an arbitrary scale. It is therefore necessary to calibrate the data in order to yield a temperature spectrum. The calibration using Virgo A works by simulating LWA-SV’s beam pattern at a given frequency on Virgo A at the midpoint of the observation. This beam pattern is then used in conjunction with the Global Sky Model (GSM; [de Oliveira-Costa et al. 2008](#)) to obtain a simulated measurement of the temperature of Virgo A at that frequency. This temperature is then divided by the arbitrary power reported by LWA-SV to generate a scaling coefficient in units of $[K / \text{Power}]$ for that frequency. This is carried out on a per frequency channel basis, in order to get a set of scaling coefficients that can be applied to the spectrum of the Science Field. These scaling coefficients are expected to be independent of the spectral structure of Virgo A and should maintain the spectral shape of the Science Field.

The accuracy of our beam models for each pointing on the sky and the accuracy of the GSM temperatures for Virgo A can obscure the calibration and induce spectral structure in the calibrated spectra. The beam model used incorporates an electromagnetic simulation of the beam pattern of a single dipole and models of the responses of the electronics along the signal path. However, it is important to note that the accuracy of the beam model is extremely difficult to verify as measuring the pattern of the entire station is a major challenge. The accuracy of the dipole simulation is also difficult to measure in the field. Possible methods of measuring the station beam pattern are discussed in Section 6. The accuracy of the GSM is dependent on frequency and position on the sky. However, at these low frequencies and Galactic latitudes, the authors report the accuracy being $\sim 10\%$ or better with respect to the input maps. [Dowell et al. \(2017\)](#) also found a similar level of agreement between a 74 MHz map made with the first station of the LWA (LWA1) and the GSM in the region of the sky near Virgo A.

4. RESULTS AND CURRENT LIMITS

The observed uncalibrated spectra of the Science Field and Virgo A are presented in Figure 4. These are the median spectra of 2 minutes of data selected from the middle of the observation described in Section 3. It is apparent that

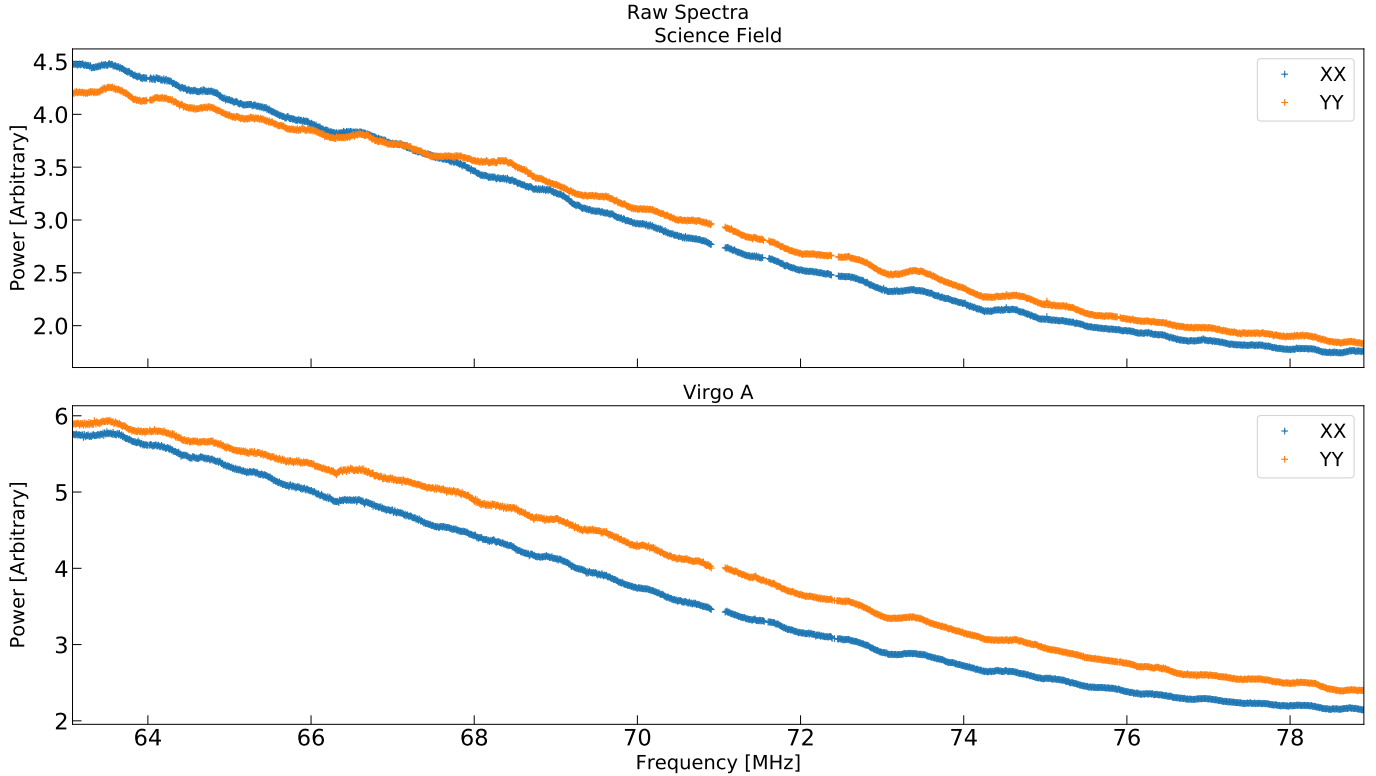


Figure 4. Raw spectra of the Science Field (top) and Virgo A (bottom) for XX and YY polarizations. These spectra consist of 2 minutes of integrated data.

the low brightness Science Field suffers from more spectral structure than the brighter Virgo A field. The scale factors derived from our calibration scheme, described in Section 3, are presented in Figure 5. These factors should help calibrate structures, whether celestial, ionospheric, or system-based in nature, and should smooth the spectra of the Science Field.

It is important to note that the scale factors do have spectral structure that we believe should not be present. The scaling should be spectrally smooth in nature, but it is clear from Figure 5 that this is not the case as many bumps are present. The source of this structure is believed to be mostly related to the chromaticity of the beam of LWA-SV. Potential sources of spectral structure which are not captured in the current temperature calibration scheme, such as beam chromaticity, will be discussed in Section 5.

The temperature calibrated Science Field and Virgo A spectra are presented in Figure 6. The spectra are generally smooth in nature with some small structure present in the Science Field spectra. These unsmooth features will not be captured by a smooth polynomial fit and will remain present in the residuals.

We investigate the performance of two foreground models of differing complexity in order to determine the extent of model dependence in the r.m.s. of the residuals. The first model we investigate is a simple power law of the form:

$$T(\nu) = k \left(\frac{\nu}{\nu_0} \right)^\alpha, \quad (4)$$

where k is a proportionality constant, ν_0 is a reference frequency, and α is the spectral index. The second model is a smooth 5-term polynomial of the form:

$$T(\nu) = \sum_{n=0}^4 a_n \left(\frac{\nu}{\nu_0} \right)^{n-2.5}, \quad (5)$$

where ν_0 is a reference frequency. We chose ν_0 to be the center frequency of the band for both models. These functions should capture the overall smooth shape of the spectrum, which is expected in this frequency regime. The best fit parameters for both models are presented in Table 2. The best fit models, with residuals, are presented in Figures 7 and 8.

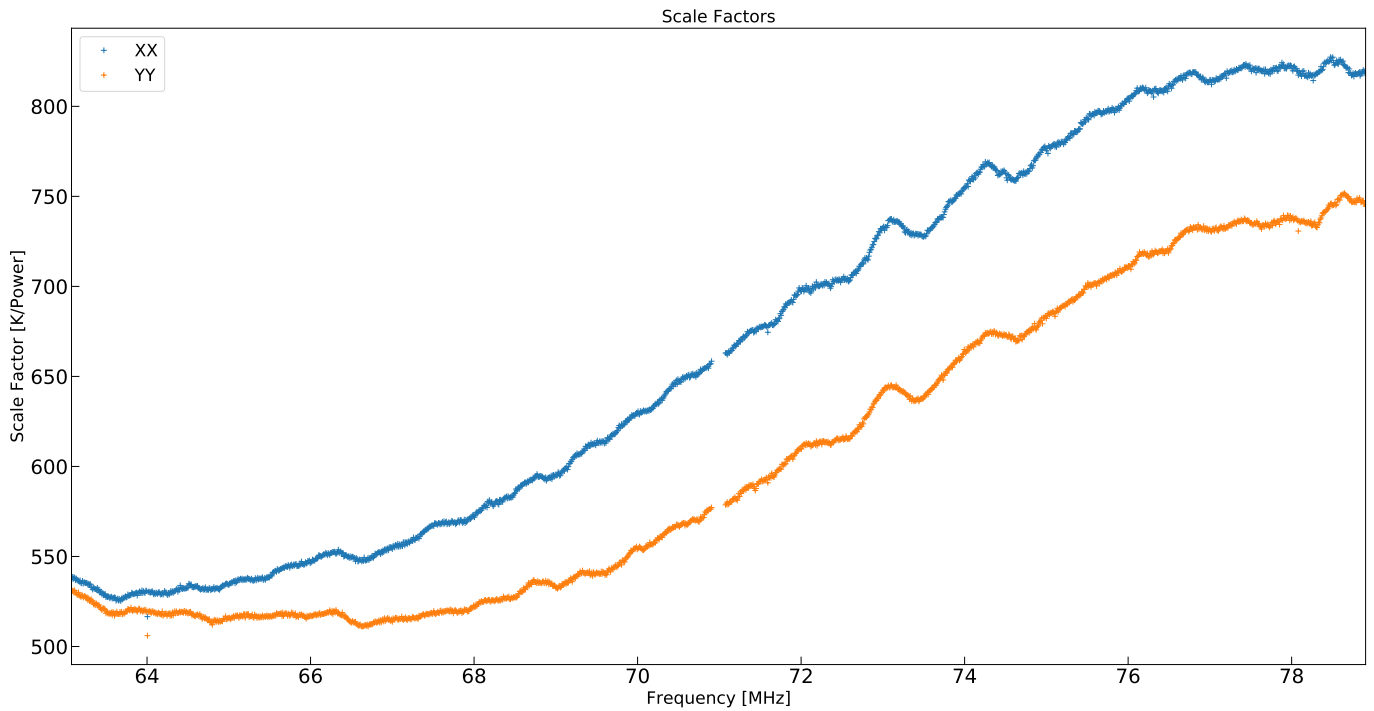


Figure 5. Temperature scale factors derived from the observed power of Virgo A and simulated beam temperatures from the Global Sky Model.

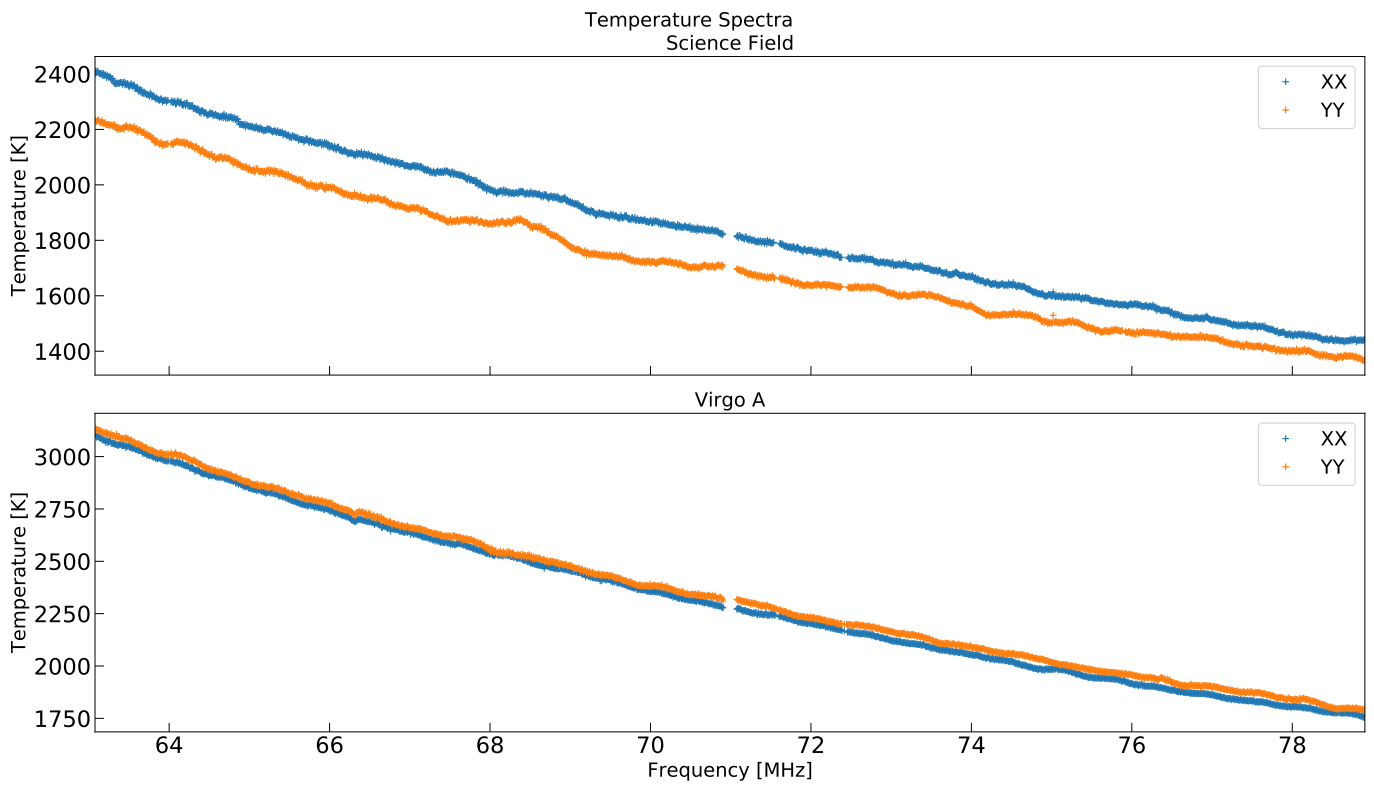


Figure 6. Calibrated spectra in units of Kelvin. These are generated by multiplying the spectra shown in Figure 4 with the curves in Figure 5.

Table 2. Foreground Model Best Fit Parameters

Model	Parameter	XX Polarization	YY Polarization
N=5 Smooth Polynomial	a_0	$7.49 \times 10^4 \pm 1.43 \times 10^4$	$2.29 \times 10^4 \pm 2.51 \times 10^4$
	a_1	$-2.69 \times 10^5 \pm 5.78 \times 10^4$	$-5.96 \times 10^4 \pm 1.01 \times 10^5$
	a_2	$3.66 \times 10^5 \pm 8.74 \times 10^4$	$5.21 \times 10^4 \pm 1.53 \times 10^5$
	a_3	$-2.18 \times 10^5 \pm 5.86 \times 10^4$	$-1.10 \times 10^4 \pm 1.02 \times 10^5$
	a_4	$4.81 \times 10^4 \pm 1.47 \times 10^4$	$-2.72 \times 10^3 \pm 2.57 \times 10^4$
Power-Law	α	$-2.26 \pm 1.89 \times 10^{-3}$	$-2.14 \pm 3.83 \times 10^{-3}$
	k	$3.26 \pm 5.36 \times 10^{-5}$	$3.23 \pm 1.09 \times 10^{-4}$

We check the performance of the system by iteratively computing the average residual r.m.s. of time-averaged spectra for different integration times, ranging from the native 80 ms resolution of the observation to 2 minutes. The data corresponding to the central 20 minutes of the observation are selected and time-averaged accordingly at each iteration to produce a number of time-averaged spectra. The foreground model is then subtracted from these time-averaged spectra and a random sample of 75% of the residual spectra are selected. We then compute the residual r.m.s. across frequencies for these residuals and compute the average residual r.m.s. across the chosen sample. This allows us to estimate the behavior of the entire distribution of residuals as a function of integration time. We look for the r.m.s. to follow a similar trend to that seen in Figure 3. This would mean that we have correctly accounted for all forms of spectral contamination both from the system and from contaminating sources on the sky. The average residual r.m.s. vs. integration time for both models is shown in Figure 9. It is apparent that the data does not integrate like unstructured data, but rather we begin to plateau after ~ 10 seconds of integration.

5. DISCUSSION

The r.m.s. of the residuals in Figures 7 and 8 are much higher than the required levels to verify the potential detection published by EDGES. In order to truly verify the claim, we require the residual r.m.s. to be at most on the order of 50 mK. This means that our reported r.m.s. level of ≈ 10 K for the XX polarization is two orders of magnitude above what we require. This high r.m.s. is likely an effect of our inability to improve signal to noise (SNR) via integration times longer than a few seconds. It is useful to break the discussion into general categories that help narrow focus onto specific issues that are contributing to the limits reported above. The issues generally fall into two categories: Calibration and Modelling.

5.1. Calibration

Figure 9 highlights that something in the system is currently prohibiting us from integrating data for long periods of time and this severely limits our SNR. The results of our initial investigation that injected a noise source into the back end of LWA-SV, summarized in Figure 3, seem to suggest that the issue is not the stability of LWA-SV back end electronics. This isolates the problem to be somewhere in either the front end electronics or the chromaticity of the station beam.

The front end of LWA-SV can suffer from issues such as the impedance mismatch between the dipoles and the FEE, standing waves between the dipoles and their ground screens, and mutual coupling between individual dipoles within the array. There have been impedance measurements made on LWA dipoles (Hicks et al. 2012), but these measurements are difficult to make for a single dipole and near impossible for the entire constructed array. Nevertheless, these models are used to take the impedance mismatch into account with the assumption that all dipoles behave the same. Standing waves between the dipoles and their ground screen would manifest as waves within the observed spectra. These should stand out in the residuals and are not seen in our spectra. Mutual coupling between elements has been shown to cause significant differences in response for each antenna, but should average out across the entire array for beamformed observations (Ellingson 2011).

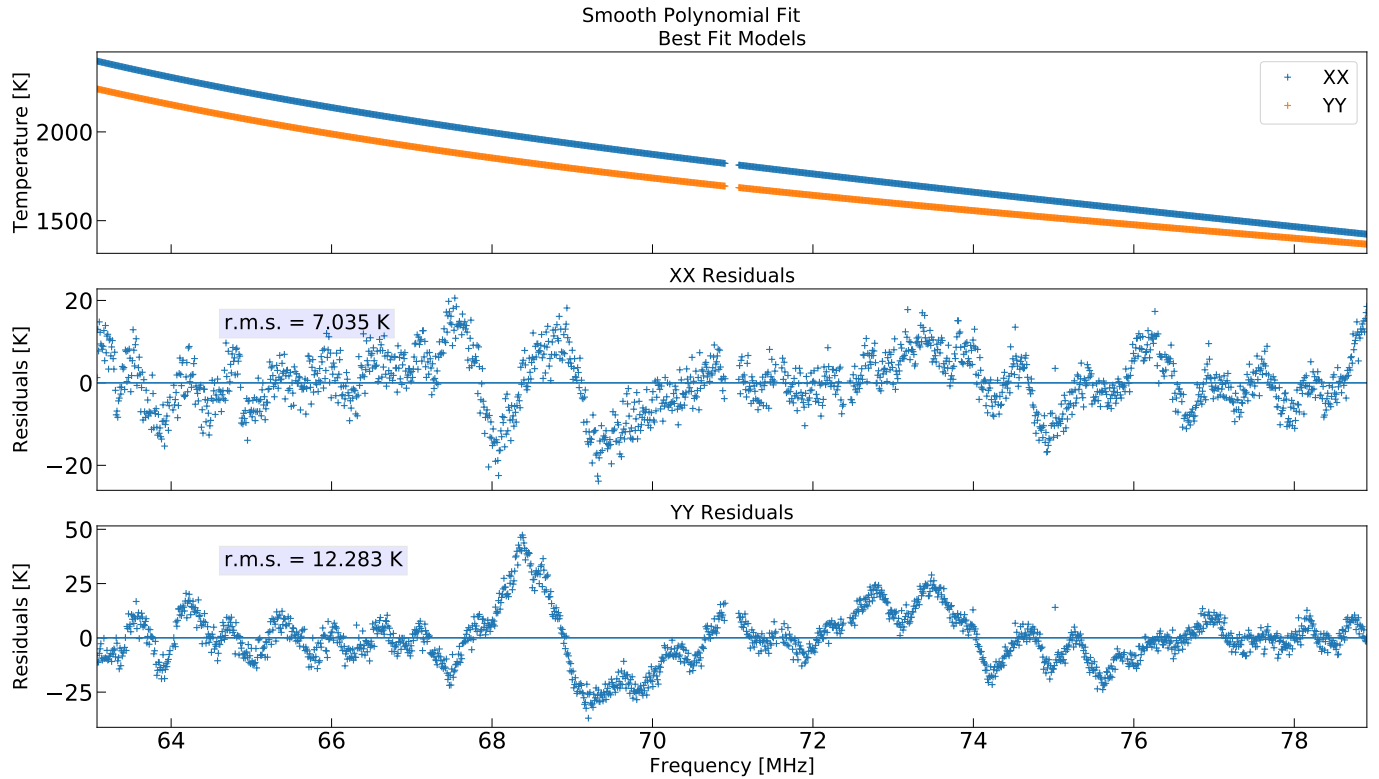


Figure 7. Best fit N=5 smooth polynomial model for each polarization. Residuals are shown in the bottom plots with zero marked with a horizontal line and r.m.s. reported in the blue box.

The frequency dependence of the dipole gain pattern⁷ and beam size contributes a major challenge for these types of experiments. This chromaticity leads to varying responses, both from the main lobe and the side lobes, with frequency which manifest as spectral features that obscure the signal. The full width at half maximum (FWHM) of the main lobe response can vary by $\approx 0.5^\circ$ across our band of $\approx 63 - 79$ MHz. The total beam pattern will also change as a function of pointing on the sky which can cause time-dependent variations in the response as the beam tracks a source over the duration of an observation. Work aiming to solve the chromaticity and directionality of the beam is presented in Section 6.

5.2. Modelling

Modelling plays a crucial role in the work presented above both in our temperature calibration and in our subtraction of galactic foregrounds. Our chosen temperature calibration scheme makes use of the GSM (de Oliveira-Costa et al. 2008) at 1° resolution; however, this is not the only sky model that we can use. The LFSS has been used to create the Low Frequency Sky Model (LFSM). This would seem to be the most logical sky model to use in order to maintain consistency of instrumentation, but the LFSM has an angular resolution of 5.1° which is currently larger than the size of the beam main lobe across our entire band. If the beam size is sub-resolution of the chosen sky model, then the temperatures derived for Virgo A will not accurately match the observed power and the scaling will be in error. The LFSM should be investigated more in the future as we further develop custom achromatic beams.

Concerns have also been raised about the GSM using a cubic-spline interpolation between input surveys which does not take physical constraints into account (Rao et al. 2017). The Global Model for the Radio Sky Spectrum (GMOSS; Rao et al. 2016) has been proposed as an alternative which takes physical constraints into account when interpolating between input surveys. However, GMOSS is also only available at 5° resolution and so we have not investigated its potential as our beam size is sub-resolution. This would lead to inaccurate temperature scaling, as stated above. Therefore, we leave the investigation into GMOSS’s performance for future work.

⁷ See LWA Memos #175 and #178.

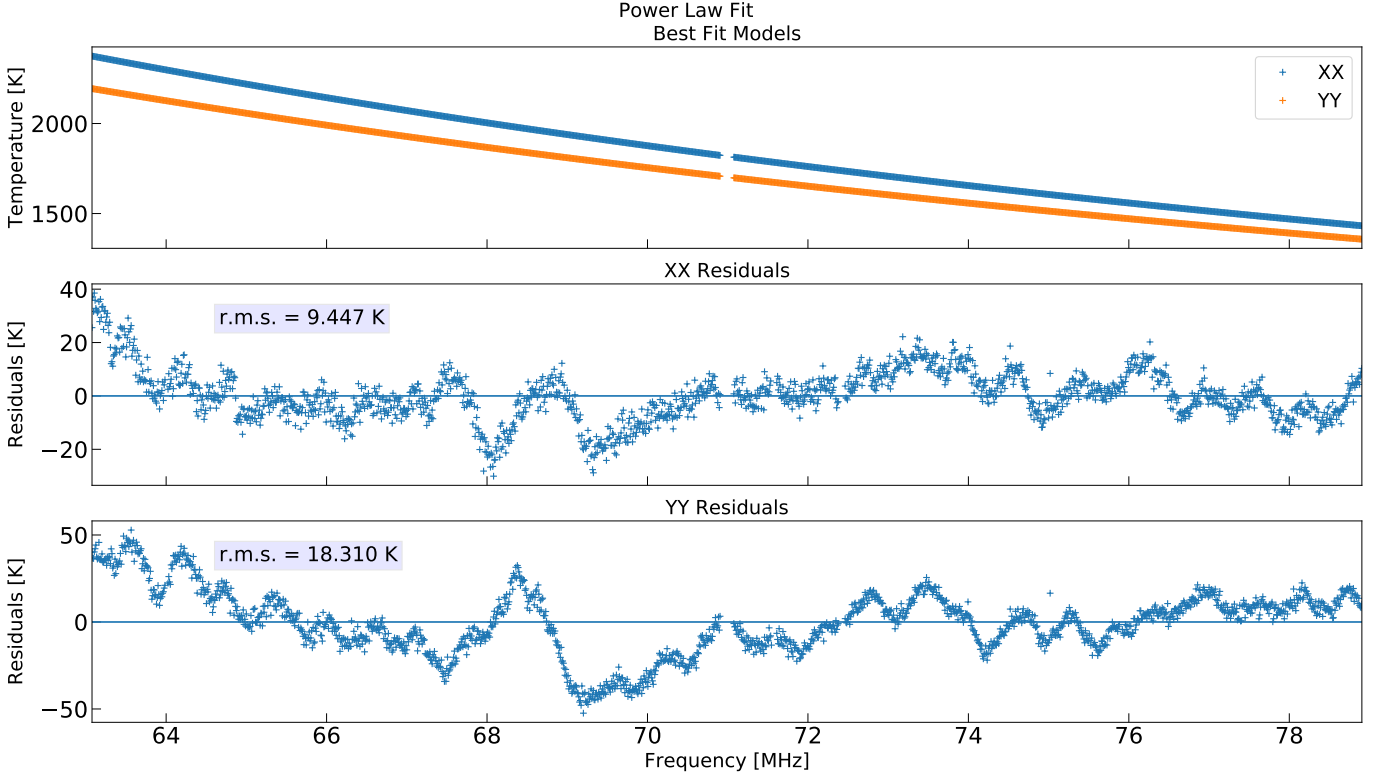


Figure 8. Best fit power law model for each polarization. Residuals are shown in the bottom plots with zero marked with a horizontal line and r.m.s. reported in the blue box.

There is also debate surrounding how to properly model Galactic foregrounds that obscure the Cosmic Dawn signal. [Bowman et al. \(2018\)](#) use a physically motivated model which accounts for galactic synchrotron emission and Earth’s ionosphere. A derivation of this physically motivated model can be found in [Hills et al. \(2018\)](#). However, [Singh & Subrahmanyam \(2019\)](#) express concerns that radiometers that observe the entire sky can produce spectra which will not be fit well by physically motivated polynomials. This is due to output spectra of the radiometer being some combination of spectra of various objects across the sky that have different spectral shapes. Thus, the output will not be well described by a single physically motivated power law. Instead, they propose the usage of maximally smooth functions ([Rao et al. 2015, 2017](#)). These should remove the smooth structure in the sky-averaged spectrum and reveal the Cosmic Dawn signal in the residuals; however, it is unclear what degree polynomial is needed to properly model systematic effects without over-modelling and washing out the Cosmic Dawn signal. It is for this reason we have looked at the performance of two different models of varying complexity in this work.

The simple power law foreground model seems to model the observed spectrum almost as well as the 5th order smooth polynomial model. The similarities between the residuals presented in Figures 7 and 8 show that most of the residual structure is on relatively small spectral scales. However, both residual r.m.s. limits presented here are overly optimistic since we have not considered the effects of signal loss due to over-modelling ([Cheng et al. 2018](#)). This is especially true for the 5th order smooth polynomial model as it will be highly correlated with smaller spectral scales. [Bernardi et al. \(2015\)](#) investigated the effects of instrumental response over a large bandwidth and found the assumption that low order foreground models will appropriately account for instrumental effects is too optimistic. They claim the signal should be detectable and will not be over-modelled by a foreground polynomial of order ≈ 5 . We expect even more on-sky structure with a beamforming approach, so a higher order polynomial model may be necessary. However, they jointly model the foreground emission and the 21-cm signal, which will account for correlations between the model parameters, and consider a much larger bandwidth than observed here. A 21-cm signal with spectral structure on the order of the bandwidth observed here can lead to large correlations between the 5th order smooth polynomial foreground model and the 21-cm signal, leading to possibly significant signal loss. These effects will be less significant

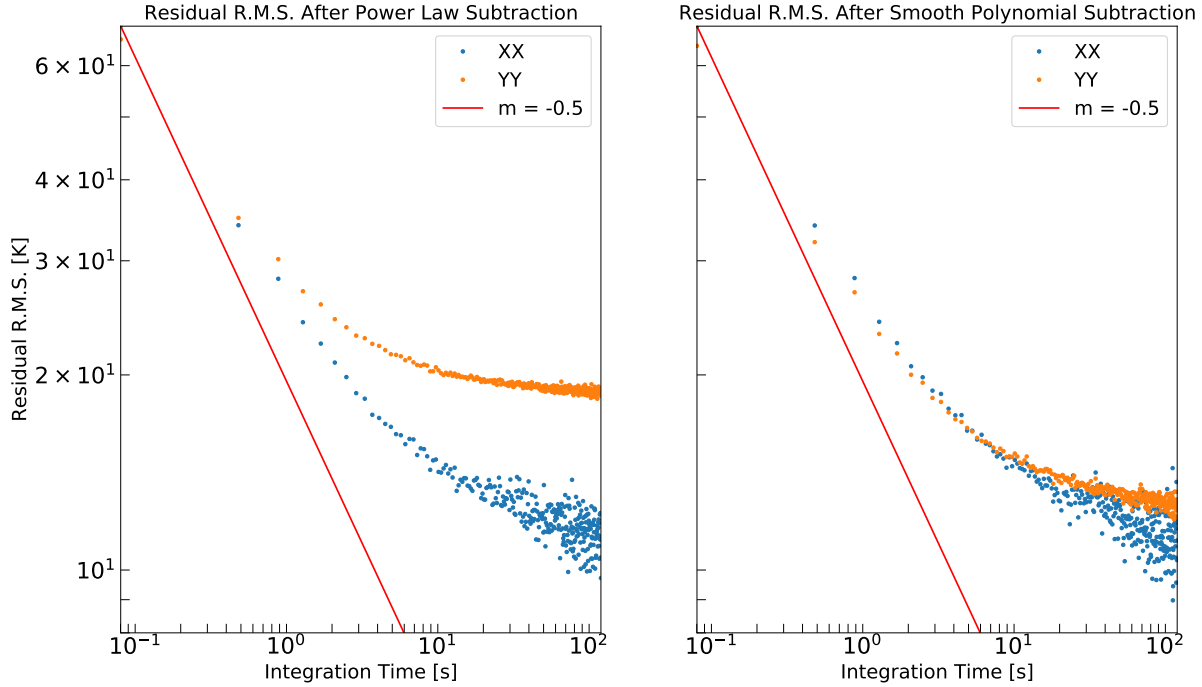


Figure 9. Average residual r.m.s. vs. integration time for each polarization. Unstructured data should go like $\sigma \propto t^{-1/2}$ (red solid line).

with a more simple foreground model like the power law shown in Figure 8. We leave a more in depth analysis of signal loss to future work.

6. CUSTOM BEAMFORMING

The chromaticity and directionality of the beam are two major sources of spectral structure for our current results. The development of a framework for custom beamforming is necessary if we wish to push our limits further into the regime where the Cosmic Dawn signal is detectable. LWA-SV offers an advantage as an antenna array since elements can be weighted in such a way to shape the beam into a custom configuration. This should allow for not only custom shaped beams for some given pointing, but also achromatic beams at that pointing across the full band. We have begun work on simulating and forming custom beams with LWA-SV. The simplest first case is to make a beam with a circular main lobe with some defined FWHM for a given frequency at any pointing on the sky. This can be achieved by weighting the array in such a way that compensates for the projection of its elliptical shape onto the sky. We begin by defining a new coordinate system, (x', y') , centered on the array with the x' - and y' -axes corresponding to directions along and perpendicular to the line of sight for a given azimuth, respectively. We then compute the physical diameter that would correspond to a defined beam width via:

$$D_1 = \frac{c}{\nu\theta}, \quad (6)$$

where c is the speed of light, ν is frequency, and θ is the user-defined beam width in radians. A second diameter is then computed which accounts for projection effects along the line of sight, given by:

$$D_2 = \frac{D_1}{\sin(e)}, \quad (7)$$

where e is the elevation of the beam pointing center. The weighting is set by defining an ellipse that is aligned with the x' - and y' -axes and has a major axis of length D_2 and minor axis of length D_1 . We apply a Gaussian taper from the

Tapered Array with line of sight FWHM of 53.1 m and perpendicular FWHM of 51.3 m for 67.0 MHz

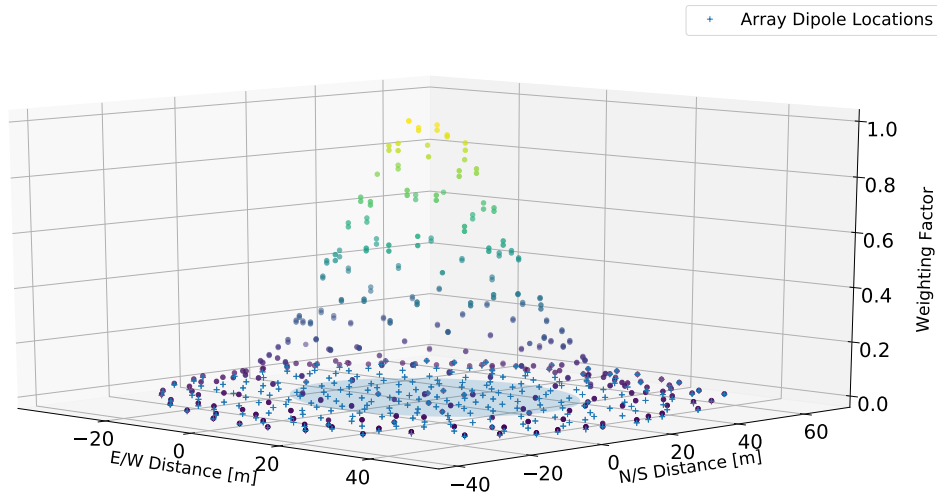


Figure 10. 3-d weighting plot showing the antenna locations (crosses) and their weight values (dots). The weighting function is a Gaussian concentric with the array. The area of the array within the full width at fifth maximum (FWFM) is shaded blue. This area has a major axis of 53.1m in the N/S direction and a minor axis of 51.3m in the E/W direction. This was generated for a pointing at 180° azimuth and 75° elevation to obtain a 5° beam at 67 MHz.

center of the array with full widths at fifth maximum (FWFM) of D_2 and D_1 along the x' - and y' - axes, respectively. An example of this weighting scheme can be seen in Figure 10.

The weighting scheme shown in Figure 10 has been computed for a pointing center located at 180° azimuth and 75° elevation for a tuning at 67 MHz. The simulated beam pattern for this weighting can be seen at the bottom of Figure 11. It is apparent from the simulations that adjusting the weights to shape the main lobe is feasible, but the cost is generally stronger side lobes, albeit the side lobes are spatially smoother. This can be an issue if a bright source enters the side lobes as a low-level Cosmic Dawn signal can be washed out. However, the main lobe becomes more isolated as the nearby side lobes seem to be pushed outward. This might be beneficial if we can make sure the response from the high side lobes is minimized by observing during times when no bright sources are in these regions of the sky.

We checked the validity of these simulations by attempting to actually generate a custom beam with FWHM of 5° at 67 MHz pointed at 0° azimuth and 83.5° elevation. This pointing allows for Cygnus A to drift through the center of the beam at its transit. We pointed the custom beam and collected data for 3 hours centered around the transit of Cygnus A to generate a drift curve. We can use the shape of the drift curve to test the shape of the beam. The results of this are shown in Figure 12. We compare the shapes of observed drift curves generated with simultaneous unshaped and shaped beams to a simulated drift curve generated using a simulation of the shaped beam pattern convolved with the LFSM. All drift curves have been normalized with respect to the peak value since the observed data is in arbitrary power units and the simulated drift curve has units of Kelvin. The LFSM has a resolution of 5.1° and so we look for similarity between the shaped beam drift curve and the simulated one. We indeed find that the shaped beam drift curve matches the shape predicted by the LFSM and therefore conclude that the beam is 5° in size.

7. FUTURE WORK

The work done thus far has highlighted potential barriers that limit our ability to integrate to the SNR required for a significant verification of the claims made in Bowman et al. (2018). We believe the largest contribution to this comes from the beam shape of the array and its chromaticity. The simulations and observations presented in Section 6 have shown that the beam is shapable, but this does not solve the chromaticity problem. In theory, this should be straight forward as we can just compute how the dipoles must be weighted for all frequencies across the band for

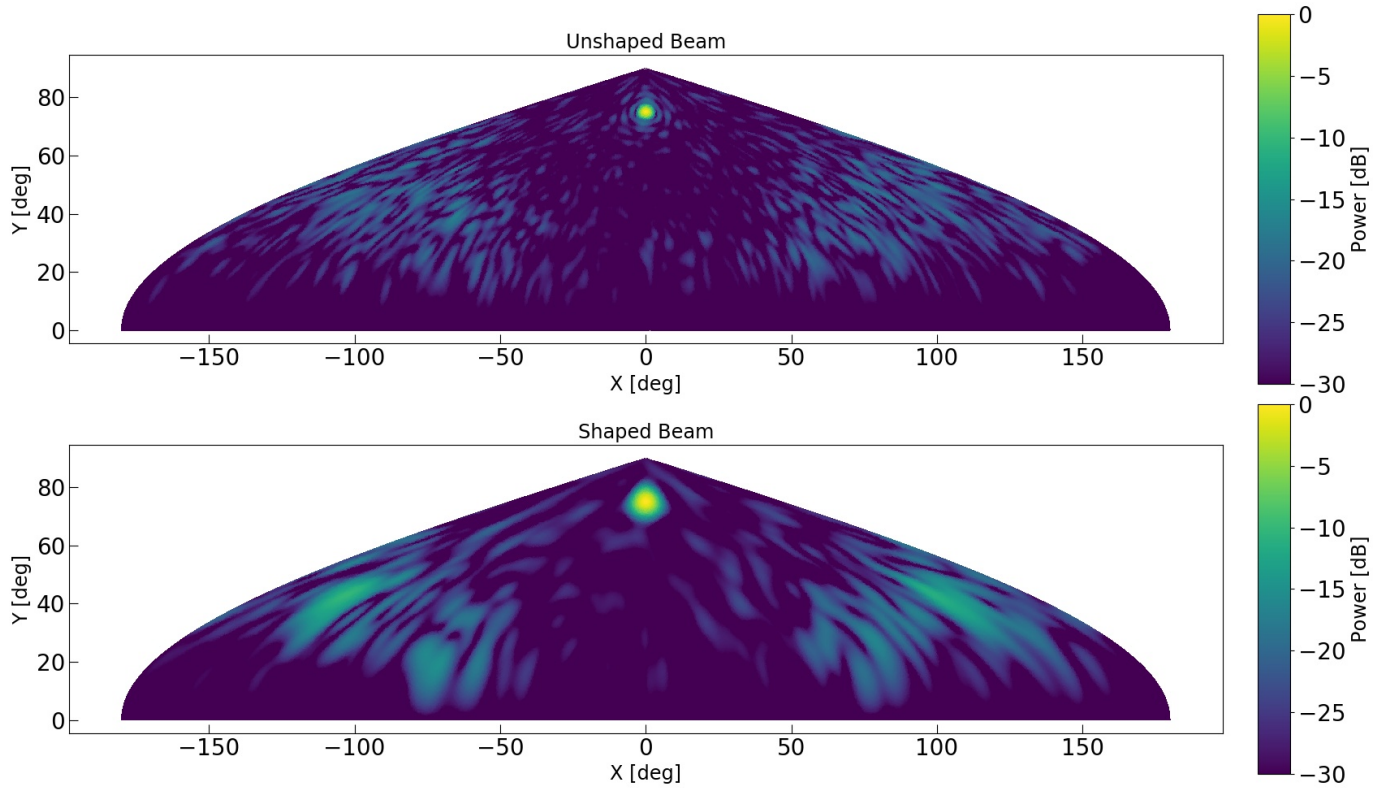


Figure 11. Simulated XX polarization beam patterns for an unshaped (top) and shaped (bottom) beam. Both patterns are for beam pointings at 180° azimuth and 75° elevation at 67 MHz on sinusoidal projection of the sky where $X = (a - a_{pointing})\cos(e)$ and $Y = e$ where a is azimuth, $a_{pointing}$ is the beam pointing azimuth, and e is elevation. The bottom plot is a circular beam with a FWHM of 5° and is a result of the weighting shown in Figure 10.

any given pointing. However, this will be more challenging in practice since the system will be required to compute and store all the weighting coefficients and apply them on a per channel basis. Implementing this into LWA-SV is in progress. Shaping the beam size will also allow us to investigate the performance of different sky models. If we choose a beam size of $> 5^\circ$, we will no longer be sub-resolution for the LWA1 LFSS and GMOSS and can properly test their performance for this application.

We also need to accurately measure the beam and dipole responses and chromaticity. This is essential if we want to verify that our beam is behaving in a way consistent with the simulations. Consistency is imperative since the simulations are necessary for our temperature calibration scheme. We have begun to experiment with measuring the dipole radiation pattern using a test drone (Chang et al. 2015; Jacobs et al. 2016). This work is underway, but this is still a new method and will need to be validated in other ways.

8. SUMMARY

We have presented first limits from LWA-SV which employs a new method for attempting to detect the global 21-cm absorption profile associated with Cosmic Dawn. These limits are still 2 orders of magnitude above what is required to validate the potential detection reported by EDGES in Bowman et al. (2018). We have detailed the stability of the system and highlighted the capabilities of a beamforming array as opposed to a single element radiometer which observes the entire sky. Simultaneous beams allow for *in situ* calibration of the system which should allow for temperature calibration which is robust against systematics such as instrumental response and ionospheric effects.

We have selected a large cold region on the sky as our Science Field and use Virgo A as a temperature calibrator. We use LWA-SV's spectrometer mode to obtain data products for the XX and YY polarizations. We are able to calibrate the observed spectrum of the Science Field and find residual r.m.s. limits of ≈ 10 K for XX polarization and ≈ 20 K for YY polarization after fitting a simple power law to model foreground structure.

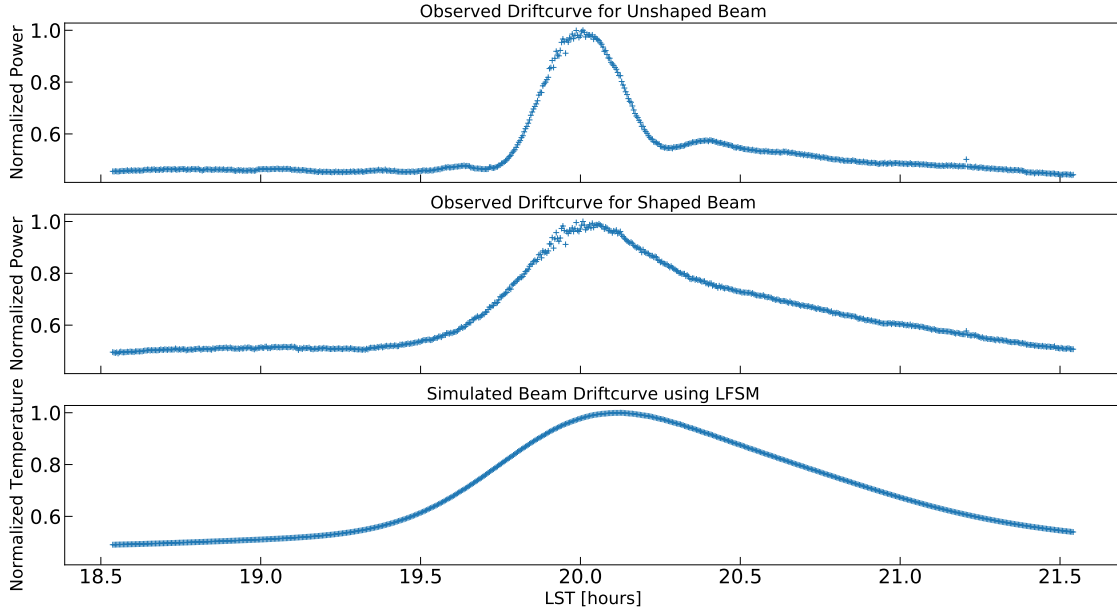


Figure 12. Observed drift curves for an unshaped beam (top) and a custom shaped beam (middle). These drift curves are centered around the transit of Cygnus A. The unshaped beam should have a FWHM of $\sim 2.8^\circ$ and the custom beam has been made to have a FWHM of 5° . It is apparent that the middle curve corresponds to a wider beam. We check the shape against a simulated driftcurve using the LFSM which inherently has 5.1° resolution. The curves have the same general shape implying the shaped beam FWHM is close to 5° .

The largest challenge that we face is the chromaticity and directionality of the dipole response and the beam. We have presented theoretical simulations and early work showing that a direction independent beam can be made and have outlined what should be needed to move forward to an achromatic beam.

ACKNOWLEDGMENTS

Construction of the LWA has been supported by the Office of Naval Research under Contract N00014-07-C-0147 and by the AFOSR. Support for operations and continuing development of the LWA is provided by the Air Force Research Laboratory and the National Science Foundation under grants AST-1835400 and AGS-1708855.

Facility: LWA

REFERENCES

- Barkana, R. 2018, *Nature*, 555, 71
- Berlin, A., Hooper, D., Krnjaic, G., & McDermott, S. D. 2018, *Physical review letters*, 121, 011102
- Bernardi, G., McQuinn, M., & Greenhill, L. 2015, *The Astrophysical Journal*, 799, 90
- Bowman, J. D., Rogers, A. E., Monsalve, R. A., Mozdzen, T. J., & Mahesh, N. 2018, *Nature*, 555, 67
- Bradley, R. F., Tauscher, K., Rapetti, D., & Burns, J. O. 2019, *The Astrophysical Journal*, 874, 153
- Chang, C., Monstein, C., Refregier, A., et al. 2015, *Publications of the Astronomical Society of the Pacific*, 127, 1131
- Cheng, C., Parsons, A. R., Kolopanis, M., et al. 2018, *The Astrophysical Journal*, 868, 26
- Cohen, A., Fialkov, A., Barkana, R., & Lotem, M. 2017, *Monthly Notices of the Royal Astronomical Society*, 472, 1915
- Cranmer, M. D., Barsdell, B. R., Price, D. C., et al. 2017, *Journal of Astronomical Instrumentation*, 6, 1750007
- de Oliveira-Costa, A., Tegmark, M., Gaensler, B., et al. 2008, *Monthly Notices of the Royal Astronomical Society*, 388, 247
- DeBoer, D. R., Parsons, A. R., Aguirre, J. E., et al. 2017, *Publications of the Astronomical Society of the Pacific*, 129, 045001
- Dowell, J., & Taylor, G. B. 2018, *The Astrophysical Journal Letters*, 858, L9
- Dowell, J., Taylor, G. B., Schinzel, F. K., Kassim, N. E., & Stovall, K. 2017, *Monthly Notices of the Royal Astronomical Society*, 469, 4537
- Dowell, J., Wood, D., Stovall, K., et al. 2012, *Journal of Astronomical Instrumentation*, 1, 1250006
- Ellingson, S. W. 2011, *IEEE Transactions on Antennas and Propagation*, 59, 1855
- Feng, C., & Holder, G. 2018, *The Astrophysical Journal Letters*, 858, L17
- Field, G. B. 1958, *Proceedings of the IRE*, 46, 240
- Furlanetto, S. R. 2006, *Monthly Notices of the Royal Astronomical Society*, 371, 867
- Furlanetto, S. R., Oh, S. P., & Briggs, F. H. 2006, *Physics reports*, 433, 181
- Furlanetto, S. R., Zaldarriaga, M., & Hernquist, L. 2004, *The Astrophysical Journal*, 613, 1
- Harker, G., Zaroubi, S., Bernardi, G., et al. 2010, *Monthly Notices of the Royal Astronomical Society*, 405, 2492
- Hicks, B. C., Paravastu-Dalal, N., Stewart, K. P., et al. 2012, *Publications of the Astronomical Society of the Pacific*, 124, 1090
- Hills, R., Kulkarni, G., Meerburg, P. D., & Puchwein, E. 2018, *Nature*, 564, E32
- Jacobs, D. C., Burba, J., Turner, L., & Stinnett, B. 2016, in *2016 IEEE Conference on Antenna Measurements & Applications (CAMA)*, IEEE, 1–3
- Mirocha, J., & Furlanetto, S. R. 2018, *Monthly Notices of the Royal Astronomical Society*, 483, 1980
- Morales, M. F., & Wyithe, J. S. B. 2010, *Annual review of astronomy and astrophysics*, 48, 127
- Muñoz, J. B., & Loeb, A. 2018, *Nature*, 557, 684
- Nita, G. M., & Gary, D. E. 2010a, *Publications of the Astronomical Society of the Pacific*, 122, 595
- . 2010b, *Monthly Notices of the Royal Astronomical Society: Letters*, 406, L60
- Parsons, A. R., Backer, D. C., Foster, G. S., et al. 2010, *The Astronomical Journal*, 139, 1468
- Price, D., Greenhill, L., Fialkov, A., et al. 2018, *Monthly Notices of the Royal Astronomical Society*, 478, 4193
- Pritchard, J. R., & Loeb, A. 2012, *Reports on Progress in Physics*, 75, 086901
- Rao, M. S., Subrahmanyan, R., Shankar, N. U., & Chluba, J. 2015, *The Astrophysical Journal*, 810, 3
- . 2016, *The Astronomical Journal*, 153, 26
- . 2017, *The Astrophysical Journal*, 840, 33
- Sims, P. H., & Pober, J. C. 2019, *arXiv preprint arXiv:1910.03165*
- Singh, S., & Subrahmanyan, R. 2019, *arXiv preprint arXiv:1903.04540*
- Singh, S., Subrahmanyan, R., Shankar, N. U., et al. 2018, *Experimental Astronomy*, 45, 269
- Sokolowski, M., Tremblay, S. E., Wayth, R. B., et al. 2015, *Publications of the Astronomical Society of Australia*, 32
- Taylor, G., Ellingson, S., Kassim, N., et al. 2012, *Journal of Astronomical Instrumentation*, 1, 1250004
- Wouthuysen, S. 1952, *The Astronomical Journal*, 57, 31